Materials Advances

ROYAL SOCIETY OF CHEMISTRY

PAPER

View Article Online
View Journal | View Issue

Cite this: *Mater. Adv.*, 2023, 4, 3330

Development of novel aspartic acid-based calcium bio-MOF designed for the management of severe bleeding†

Chandan Bhogendra Jha,[ab] Chitrangda Singh,[a] Raunak Varshney,[a] Sweta Singh,[a] Kuntal Manna *[b] and Rashi Mathur *[a]

Received 2nd February 2023,
Accepted 27th June 2023

DOI: 10.1039/d3ma00061c

rsc.li/materials-advances

Haemostatic agents must play a key role in managing severe bleeding conditions during trauma or battlefield. Using natural ligands and bioactive metals, we can design materials that can enhance innate haemostatic capability. This study entails the synthesis of amino acid-based MOF using L-aspartic acid as an organic ligand and calcium as a metal node, where the parametric optimization is made using a Box-Behnken experimental design. Out of the total experimental runs obtained, the one with the highest reaction yield was evaluated. It was observed that despite low porosity and surface area, the impact of the synthesised Ca-MOF on the haemostatic property was very high. A haemolysis ratio <1.55%, which induces erythrocyte absorption and aggregation, activated the intrinsic coagulation pathway and accelerated blood coagulation as assessed using TEG. The evaluated Ca-MOF shows the shortest clotting time (39 ± 0.2 s) and lowest blood loss (0.14 ± 0.2 g) in the rat-tail amputation model compared to the control and commercially available haemostatic drug tranexamic acid. With the enhanced coagulation capacity and associated biocompatibility, the developed calcium-aspartate bio-MOF could act as a safe and effective haemostatic agent and provide a unique concept for using synthetic porous materials for the management of excessive bleeding.

Introduction

Metal–organic frameworks are a potential class of crystalline hybrid materials with unique features such as large pore volume and high surface area that are useful in various applications.[1,2] Most metal–organic frameworks (MOFs) have distinct scaffolding architectures with big pores.[2,3] These distinguishing characteristics make this hybrid material a viable choice as a drug carrier.[4] MOFs are frequently compared to the porous structure of sponges on a nanoscale.[5] These pores can encapsulate other molecules, such as active medicinal compounds or enzymes.[6] Furthermore, the ligand molecules connecting the metal ions provide open binding sites. This indicates that we can attach additional molecules to the scaffolding structure of MOFs, which gives us the flexibility to use MOFs for different applications.[6–8] To the best of our knowledge, MOFs have been examined for medical purposes, but none have been extensively commercialised. This is not surprising as extensive clinical testing methods are required because MOFs have only been extensively evaluated since their identification in the late 1990s.[8,9] To synthesise biocompatible MOFs, it is important that both the inorganic metal and organic linker exhibit low toxicity. High-valent earth-abundant metal ions (*e.g.*, Al^{3+}, Fe^{3+}, Ti^{4+}, or Zr^{4+}) exhibit long-term stability in their complexes because they are considered harmless to the human body and have become a preferable choice for inorganic nodes in MOFs.[7,8] These MOFs have high charge densities to form stronger coordination bonds and enhance the stability of MOFs.[10] Similarly, many of the alkali or alkaline earth metal-based MOFs are also biocompatible; however, their MOFs are very scarce as the bonding interaction of metal–ligand is ionic owing to electronegativity differences, which results in difficulty in controlling coordination geometry and steric considerations.[11] Calcium is among the most abundant elements on the earth's crust, which is nontoxic in nature, very cheap and known to have biological importance, and this unique feature of calcium favours the synthesis of calcium-based MOFs for various biomedical applications.[11]

α-Amino acids can be used as organic linkers because they are naturally occurring biocompatible compounds and are also suitable to form coordination with various metal ions *via* a range of chemical conditions.[12–14] However, pure α-amino

[a] *Division of Radiological, Nuclear and Imaging Sciences, Institute of Nuclear Medicine and Allied Sciences, DRDO, Lucknow Road, Timarpur, Delhi 110054, India. E-mail: rashimathur07@gmail.com*
[b] *Department of Chemistry, Indian Institute of Technology, Delhi 110016, India. E-mail: kuntal.manna@chemistry.iitd.ac.in*

† Electronic supplementary information (ESI) available. See DOI: https://doi.org/10.1039/d3ma00061c

acids based on divalent transition metals and main group metals or rare earth metals are rarely reported,[15] and others with three-dimensionality (3D) and accessible porosity are much scarcer. This could be attributed to the influence of the common chelating coordination fashion of α-amino acids.[15] Out of the known 20 standard L-α-amino acids, aspartic acid is the smallest one assigned with two carboxylate groups with a separation distance, which is appropriate for energetically favourable robust bridging/linkage of inorganic nodes. Some of the crystal structures of metal-aspartate MOFs, which have been reported thus far, show limited hydrolytic stability.[16–21]

In this study, we synthesised a bio-MOF of calcium-aspartate and investigated its capability to manage severe bleeding. To the best of our knowledge, process optimisation data for Ca-MOF synthesis using experimental design statistical techniques have not been reported in the literature. The synthesis was performed under optimised conditions suggested by the Box-Benhken design (BBD), followed by the experimental run of the reaction, which shows the highest percentage of reaction yield. The reaction product was physio-chemically characterised using analytical techniques to establish the nature of the Ca-MOF synthesised in terms of size, surface area, porosity and structure. In addition to this, the blood compatibility, interaction with different clotting proteins and their *ex vivo* haemostatic performance in static and dynamic conditions were also evaluated. The *in vivo* haemostatic performance owing to its potential use in managing excessive bleeding was evaluated using tail amputation models in Sprague–Dawley (SD) rats.

Experimental

Chemicals and reagents

All chemicals were purchased from Sigma-Aldrich and were used without any further purification unless and until mentioned. Calcium chloride dihydrate ($CaCl_2{\cdot}2H_2O$ AR 99.99%), L-aspartic acid ($C_4H_7NO_4$ AR 99.99%), human serum albumin (purity > 98%), gamma globulin (purity > 98%), fibrinogen (purity > 98%), plasminogen (purity > 98%), tris–HCl (purity > 99%), methanol (CH_3OH AR 99.8%) deionized water and Vacutainers (Levram Lifescience, Silvassa, India).

Quality by design approach

The objective behind using Box-Behnken Design (BBD) with three levels for each factor is to introduce researchers to a design space of independent variables prior to designing experimental runs to save time and effort and to reduce precision errors. This design space serves as a statistical model for screening or making initial comparison and identification of the important synthesis variables (such as temperature, reactant concentration, and time). Finally, the ANOVA analysis of the design space optimized the response variable with the aim of attaining the maximum yield based on the model equation developed with the most significant factors. By utilizing the results obtained from model validation with significant differences between actual and predicted response values, researchers can design their experiments with minimum material loss and save time.

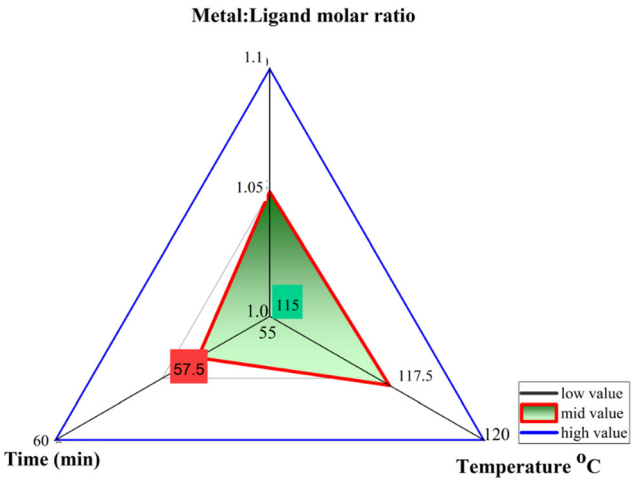

Fig. 1 Independent factors and their levels used in the Box-Behnken design.

The optimization of process parameters for Ca-MOF synthesis was examined through BBD experimental design (3 factors, 3 levels) in response surface methodology by Design-Expert Version 10.0.[22] Metal: ligand ratio, time, and temperature with their low and high levels (Fig. 1) were modelled as independent variables using 17 experimental runs, as shown in Table 1, to predict the performance of the dependent variable, *i.e.*, percentage reaction yield. Herein, 3D response surface plots depict the influence of predetermined factors on the percentage reaction yield.

Method of synthesis

Synthesis of Ca-MOF. The reaction conditions for synthesising calcium-based MOF were optimised using the BBD statistical tool. We carried out the experimental run for reaction conditions that showed maximum yield. Briefly, L-aspartic acid

Table 1 Design matrix of the Box-Behnken design for Ca-MOF synthesis

	Factor 1	Factor 2	Factor 3	Response 1
	A: Ca : L-aspartic acid	B: Temp	C: Time	Product Yield
Run	Molar ratio	°C	Minute	%
1	1	120	57.5	59
2	1.05	117.5	57.5	63
3	1.05	115	60	57
4	1.05	115	55	55
5	1	117.5	55	58
6	***1.05***	***120***	***60***	***66***
7	1.05	120	55	58
8	1.05	117.5	57.5	63
9	1.1	117.5	55	58
10	1.1	115	57.5	54
11	1.1	117.5	60	62
12	1.1	120	57.5	59
13	1	115	57.5	54
14	1	117.5	60	62
15	1.05	117.5	57.5	63
16	1.05	117.5	57.5	63
17	1.05	117.5	57.5	63

(20 mmol) was taken in a round bottom flask and dissolved in excess water to give a suspension. Simultaneously, in a separate flask, $CaCl_2{\cdot}2H_2O$ (15 mmol) was dissolved in water to give a clear solution. This was followed by gradually adding the metal salt solution to the aspartate suspension for over half an hour with continuous stirring to obtain a clear solution (total volume of 25 ml). This solution was then transferred to the autoclave for hydrothermal heating (120 °C, 60 min). The reaction mixture was cooled to room temperature, centrifuged, washed with water three times to remove unreacted reactants, and then vacuum dried at 60 °C.[23,24]

Analytical characterization

Powder XRD analysis was used to obtain the crystallography of the synthesized Ca-MOF (Bruker's X-ray Diffractometer, D8) with Cu Kα as the X-ray source, and the scan range was 5°–100° 2θ degrees at a step of 0.01° minute^{-1}. The morphology of the Ca-MOF was examined using SEM in a (TESCAN MAIA 3) at 5.0 kV high voltage using tungsten detectors at an angle of 45°. AFM studies were performed using a Bruker-JPK Instrument, Nanowizard III (JPK Instruments AG, Berlin, Germany). Transmission electron microscopy (TEM) images of Ca-MOF were taken using JEOL JEM-1400 equipped with STEM at an accelerating voltage of 300 kV. An atomic absorption spectrometer (AAS) equipped with a short-arc xenon lamp, a continuous radiation source, and a double echelle grating monochromator connected with a charge-coupled device array detector was used (LAB-India 800, India) to calculate the metal contents. The TGA was measured to understand the thermal stability and degradation pattern (TGA 5500, USA). The thermograms were measured in a continuous N_2 flow of 50 ml minute^{-1} from 50 °C to 900 °C at a heating rate of 10 °C minute^{-1}. An FTIR spectrophotometer was used to check conjugation (Cary 630, Agilent Technologies, USA). Samples were prepared using the KBr pellet methods and scanned at wavelengths ranging from 500 to 4000 cm^{-1}. The specific surface area, pore volume, and pore diameter were measured using a BET instrument (Quantachrome NOVA 2200, USA). Prior to the study, the samples were vacuum dried at 80 °C for 24 hours and degassed for 6 hours. DLS and Zeta potential (Malvern Zetasizer ZS 90) measurements were performed to determine the hydrodynamic diameter and net surface charge of the synthesized Ca-MOF. The samples were diluted with water before being measured in triplicate at room temperature and in the pH range of 5.0–6.5. The stability of the samples was also checked under different pH conditions. The fluorescence emission spectra were recorded using a Gen5 fluorescence spectrophotometer (BioTek USA).[23–28]

Biocompatibility studies

Evaluation of blood cell integrity. To investigate the alterations in blood cells caused by Ca-MOF, we performed a blood cell integrity study based on reported literature.[29] In brief, 1 mg of material was incubated for 30 minutes at 37 °C with whole blood (1 ml) containing 20 μl EDTA as an anticoagulant at 400 rpm. Similarly, an equivalent volume of whole blood was incubated without any test material that served as the control. Following incubation, peripheral blood smears were prepared and fixed in 100% methanol (CH_3OH) for 3 minutes. This was followed by Giemsa staining diluted in distilled water (1 : 9) for 20 minutes. After rinsing the dried smears in water, they were scanned in triplicate using an optical microscope (Olympus BX51, camera: DP71) (n = 3).

Haemolysis analysis. The (ASTM F-756-00, 2000) standard was used to calculate percentage haemolysis.[29,30] The relative amounts of haemoglobin were released into the solution phase from the erythrocytes after being subjected to the test materials. 1 mg of Ca-MOF was incubated with 1 ml of fresh human blood, which was diluted with 7 ml of PBS. The mixture was then incubated for 15 minutes at 37 °C before being centrifuged for 5 minutes at 800 rpm. The supernatant was collected to evaluate haemolysis. The UV/Vis Spectrophotometer (PerkinElmer Lambda365) was used to determine the absorbance at 540 nm. Negative controls were 1 ml diluted blood in 7 ml normal phosphate buffer saline, while positive controls were 1 ml blood in 7 ml DI water.

$$\%\,\text{Haemolysis} = \frac{\text{Absorbance of sample} - \text{Negative control}}{\text{Positive control}} \times 100 \quad (1)$$

Cell viability assay. Two different cell lines, namely L929 fibroblast cells and human epithelial A549 carcinoma cell lines, were used to check the relative cellular viability of Ca-MOF. Both cell lines were cultured in 96-well plates with 200 μL of media per well and treated with Ca-MOF concentrations ranging from 30–1000 μg ml^{-1}. The media were withdrawn after treatment, and the cells were rinsed twice with PBS (pH 7.4) at 37 °C before being placed in fresh PBS. The MTT solution was then added to the cells at a concentration of 1 mg mL^{-1}, and the cells were cultured under usual conditions for 24 and 48 h. PBS was withdrawn after incubation, and DMSO was added to dissolve the generated formazan crystals. A micro-plate reader (Multiskan GO, Thermo Scientific, India) was used to measure the optical density of formazan solution in DMSO at 540 nm. Cell viability was measured at each concentration point as the ratio of the mean optical density of repeated wells to that of the negative control.[31,32] The experiment was carried out in triplicate.

***In vitro* protein interaction studies.** Interaction of Ca-MOF with different proteins found in blood (Human serum albumin, plasminogen, fibrinogen and gamma globulin).

The interaction of Ca-MOF with different proteins was studied using the fluorescence quenching method. The fluorescence emission was measured from 300 to 600 nm at an excitation wavelength of 280 nm, at 2 nm interval, and slit widths of 10 nm. Each spectrum was measured in triplicate. To adjust the fluorescence background, PBS was utilised as a fluorescence emission blank. In brief, the fluorescence intensity (F0) of the native proteins, namely, HSA, Plasminogen, Fibrinogen and Gamma Globulin, is first measured. Then, keeping the concentration of the protein fixed (150 mol L^{-1}, in PBS pH 7.4), varied concentrations of the Ca-MOF (namely, 50 μg ml^{-1}, 125 μg ml^{-1}, 250 μg ml^{-1}, 500 μg ml^{-1} and 1000 μg ml^{-1}) was added to the protein solution. The mixture was incubated in the wells of a microtiter plate for 1 h at 298 K. No separation processes

(such as centrifugation or filtration) were utilised in the experiment to avoid shear pressures from altering the structure of the bio conjugates.[33,34] All experiments were carried out at room temperature and in triplicate. The Stern–Volmer equation was utilised to determine the dominant quenching mechanism. The equilibrium binding constant (K_q) in protein–MOF interaction studies can be calculated using the fluorescence quenching method:

$$\frac{F_0}{F} = 1 + K_q\tau_0[\mathrm{MOF}] = 1 + K_{SV}[\mathrm{MOF}], \quad (2)$$

where F_0 and F denote the relative fluorescence intensities of the proteins in the absence and presence of Ca-MOF, respectively; [MOFs] denotes the concentration of Ca-MOF; K_q denotes the quenching rate constant; K_{SV} denotes the Stern–Volmer dynamic quenching constant, which is related to the bimolecular collision process and τ_0 denotes the lifetime of a fluorophore in the absence of quenchers (10^{-8} s).[35] The association constant (K_a) and the number of binding sites (n) may be determined using the following equation assuming that the proteins have an identical and independent binding site:

$$\log\left[\frac{F_0 - F}{F}\right] = \log\ K_a + n\log[\mathrm{MOFs}], \quad (3)$$

where $\log\left[\frac{F_0 - F}{F}\right]$ was plotted against log [MOFs] (Fig. 9) based on the experimental results and the number of binding sites for all proteins.

Ex vivo studies

Assessment of whole blood clotting time (CT). The experiment was performed in accordance with earlier reported literature;[36,37] CT was calculated by taking test materials (500 μg ml^{-1}) in Eppendorf tubes. Collection tubes were placed in a water bath at 37 °C for 10 minutes before being observed for blood coagulation. Blood was drawn from a healthy participant with informed consent according to Helsinki principles. 3.8% of anticoagulant was used to prevent blood coagulation. The tubes were filled with 340 μl of whole blood. The sample was then warmed to 37 °C in a water bath, and 0.2 M $CaCl_2$ (20 μl) was added. The tubes were inverted every second and held in a position before reverting. CT was defined as the time when no flow of samples was detected. In all tubes, the CT was calculated as a function of the time from the start of blood collection to the end of blood coagulation. All the measurements were performed in triplicate. The control was measured without the use of test materials. The Ca-MOF was gently rinsed thrice in PBS to remove the clot after haemostatic testing, and the Ca-MOF was studied under scanning electron microscopy.

Plasma recalcification time (PRT). PRT was measured using the procedure reported earlier.[36,37] Blood was collected from a healthy donor in an anticoagulant sodium citrate (9 : 1) vial. The obtained samples were centrifuged at 4 °C and 2000 rpm for 10 minutes to obtain platelet poor plasma (PPP). Fresh 300 μl of PPP were incubated for 3 minutes at 37 °C with 500 μg ml^{-1} of test material. 30 μl of 0.5 M $CaCl_2$ was used to recalcify the plasma. The fibrin thread development in PPP was carefully observed in the plasma. PRT was defined as the time taken for the $CaCl_2$ to recalcify after it was added.

Platelet adhesion. Platelet adhesion was measured using the method reported earlier.[36,37] Platelet-rich plasma (PRP) was collected by centrifuging whole blood treated with 3.8 percent sodium citrate at 4 °C for 10 minutes at 2000 rpm. The Ca-MOF was incubated with 650 μl of PRP at 37 °C for 1 h. It was then rinsed in 0.1 M PBS to remove plasma proteins and nonadhered platelets, fixed for 1 h with a 2% glutaraldehyde solution, dehydrated with ethanol, dried at ambient temperature and stored in desiccators. Scanning electron microscopy was used to examine platelets adhering to the material.

Thromboelastographic (TEG) studies. To understand the hemostasis process and where the material impacts, TEG studies were performed as per an earlier reported protocol.[38–42] Measurement of Ca-MOF concentrations ranged from 50 μg ml^{-1} to 1000 μg ml^{-1} using whole blood as control was performed. Specific to this study, blood samples were obtained from healthy volunteers after obtaining consent as per the institutional ethical committee guidelines (ECR/824/Inst/DL/2016/RR-19) through venipuncture and collected into separate vacutainers with 3.2% sodium citrate solution and gently inverted three times. For the TEG analysis, the citrated whole blood was kept at room temperature for 30 minutes. The TEG5000 (Steranco Health Care Pvt. Ltd) system was used to perform thromboelastographic measurements. Using a TEG cup preheated to 37 °C, a Ca-MOF solution (50 μl) made at varied concentrations in the Tris buffer was loaded into the cups. Calcium chloride solution (20 μl) and blood (310 μl) were then added to the same TEG cup, which contained a 0.2 mol L^{-1} solution of calcium chloride. After pipetting the whole solution in and out once to mix it equally, the measurement was initiated. The calcium chloride solution was mixed with citrated human blood and taken as a control. Analysis was carried out until all the relevant parameters (*i.e.*, R, K, α, MA, and TMA) were measured. All the measurements were carried out at 37 °C and in triplicate.

***In vivo* homeostasis studies.** All *in vivo* studies were carried out in accordance with the protocol approved by the institutional animal ethics committee (INM/IAEC/19/01/Ext.1 dated 02-09-21). All experiments were carried out on male SD rats (8–10) weeks old. The animals were maintained under typical conditions (12/12 h light and dark, with access to water and food) until the process was completed. A rat tail amputation model was used to assess its haemostatic effectiveness. In brief, healthy male Sprague–Dawley rats were separated into three groups: control, treatment and standard (tranexamic acid). Ca-MOF and tranexamic acid at an equivalent concentration of 500 μg ml^{-1} with 1 ml volume were administered intravenously through the tail vein. After one minute of intravenous administration of Ca-MOF and tranexamic acid, an incision was performed 4 cm below the tail using a sterile blade. At 37 °C, the severed tail was submerged in sterile saline. After the bleeding stopped, the tail was continued to submerge in warm saline for 4 minutes to watch for any subsequent bleeding episodes. The bleeding time and weight of blood loss were recorded.[29,43–45]

Statistical analysis

All the observations are presented as average ± standard deviations. All experiments were carried out in triplicate, and data were generated accordingly. In all the studies, the value of $P < 0.05$ was statistically significant.

Results and discussion

Quality by design approach

According to the suggested model, which fitted well to the experimental data, the results obtained are given in the following mathematical equation (in coded terms):

$$\text{Product yield (\%)} = +62.89 + 0.000 \times A + 2.75 \times B + 2.25 \times C + 1.50 \times \text{BC} - 2.76 \times A^2 - 3.76 \times B^2. \quad (4)$$

This equation represents that as the ratio of factor B (temperature) and C (time) increases, the reaction yields increase, whereas factor A (molar ratio of Ca : L-aspartic acid) had lower significance with the interaction between time and temperature together, and a significant increase in reaction yield was observed initially up to some extent after which there was no significant improvement in the product yield. This is also supported by the 3D surface response and contour plots, as shown in Fig. 2, which are obtained by varying two significant factors, while keeping the third factor constant, showing the geometry of the response as it can be clearly seen that yield would be strongly increased for high temperature. The adequacy of the selected quadratic model was investigated by performing statistical runs, such as analysis of variance (ANOVA), (Table S1, ESI†) analysis of residuals and coefficient of determination. All the factors and their interactions are significant (P value ≤ 0.05). The R^2 (0.9939), $R_{adj}{}^2$ (0.9903) and $R_{predicted}{}^2$ (0.9627) with close values confirm the adequacy of the proposed model (Table S2, ESI†). The statistical error analysis was performed using a normalized standard deviation. The optimized conditions for maximizing yield are shown in Table 2.

Table 2 Predicted and observed values for the optimized Ca-MOF

Factor	Optimized level
Ca : L-aspartic acid	1.05 (ratio)
Temperature	118 (°C)
Time	58 (minutes)

Response	Expected	Observed	Residual
Reaction yield	64.6091	65.67	1.0609

Physicochemical analysis of the prepared metal organic framework

The XRD spectra of the as-synthesized Ca-MOF, native L-aspartic acid, and metal salt ($CaCl_2{\cdot}2H_2O$) are shown in Fig. 3. The prominent peaks for Ca-MOF were observed at 2θ values of 23.73°, 35.95° and 48.63° corresponding to (111), (211) and (222) planes, respectively. The diffraction d-spacing is in good agreement with the d-spacing calculated using the SAED pattern of TEM images at 0.37 nm and 0.187 nm, which corresponds to the (111) and (222) planes of Ca-MOF, respectively, with an average grain size of 40 nm. Moreover, the peak broadening observed in the XRD pattern for the $CaCl_2{\cdot}2H_2O$ from 0–25° may be owing to the lattice strain and dislocated unit cell as the dihydrate form of calcium chloride, especially at room temperature, undergoes rapid hydration even after prior activation. The SEM images show a plate-like morphology for the Ca-MOF. The plate-like morphology of the Ca-MOF has a 3D configuration, as shown in the SEM (Fig. 3(b) and (c)). Further in the AFM images (Fig. 3(d)–(h)), it was observed that the sample show crystals grown over a thin film-like structure. The crystals demonstrate a multi-layered structure, showing a height of approximately 15–20 nm, as shown in the height profile.

The TEM image (Fig. 4(a)) shows MOF particles of approximately 200 nm diameter that agree well with the DLS, which shows a size of approximately the same size 210 nm (Fig. 4(e)). TEM EDS mapping shows the presence of Ca, C, O and N (Fig. 4(c) (inset)), and the corresponding EDS spectra are shown

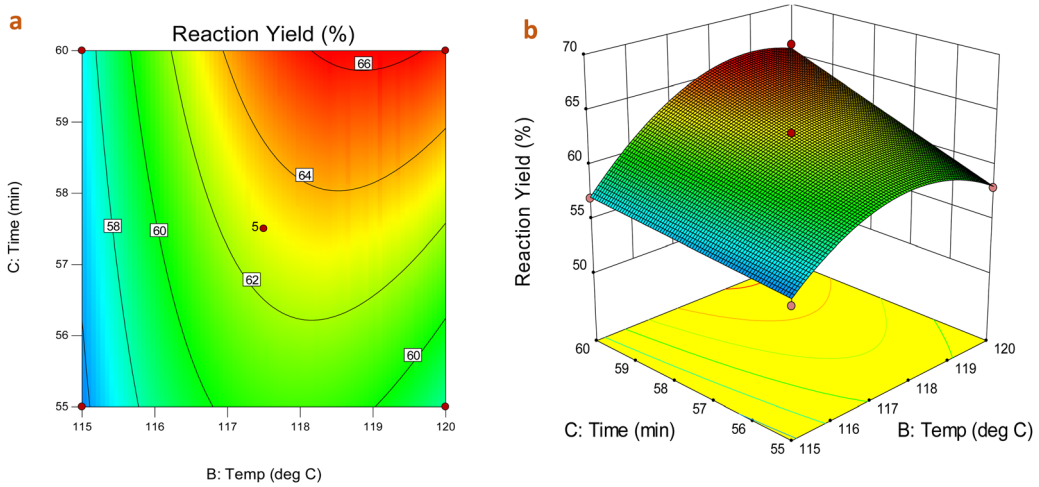

Fig. 2 (a) Contour plot (b) 3D surface plot of product yield as a function of temperature, time and their mutual interaction over product yield at fixed metal : ligand molar ratio.

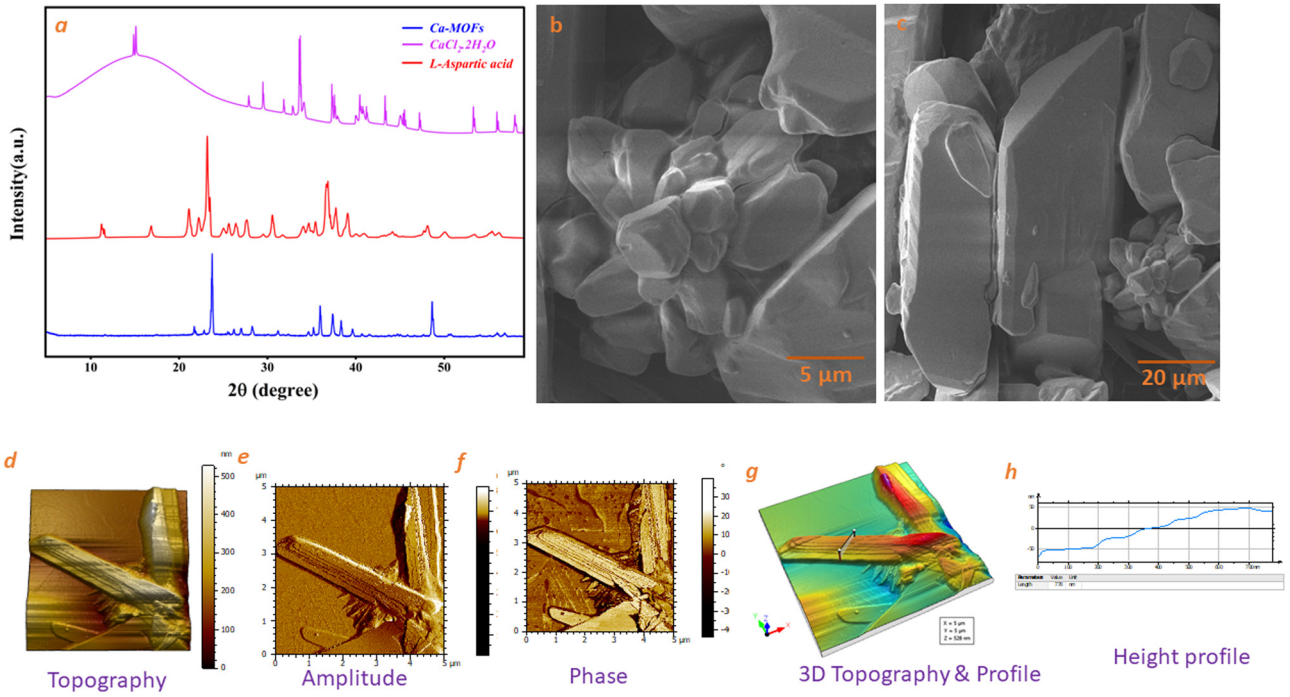

Fig. 3 (a) PXRD pattern of Ca-MOF, L-aspartic acid, $CaCl_2{\cdot}2H_2O$ (b) and (c), SEM images of Ca-MOF at different magnifications of 5 µm and 20 µm. AFM Images of Ca-MOF (d) topography (e) amplitude (f) phase (g) 3D topography & profile (h) Height Profile.

in Fig. 4(c). The presence of Ca was also confirmed by atomic absorption spectroscopy (AAS), which was estimated at about 6.241 (wt%) as interpreted from AAS data.

The thermal stability of the as-synthesized Ca-MOF after sample activation was characterized using a thermogravimetric instrument (Fig. 5(a)). According to TGA results, removal of free water molecules from the surfaces of MOF occurs in the temperature range of 220–267 °C, and second mass loss of up to 34% in the temperature range of 267–393 °C results from the evaporation of adsorbed water molecules and partial decomposition of organic ligand. Beyond this temperature, the MOF structure collapses.

The FT-IR spectrum of the synthesized Ca-MOF is presented in Fig. 5(b). The peaks at 3308 cm^{-1}, 1152 cm^{-1} and 1047 cm^{-1}

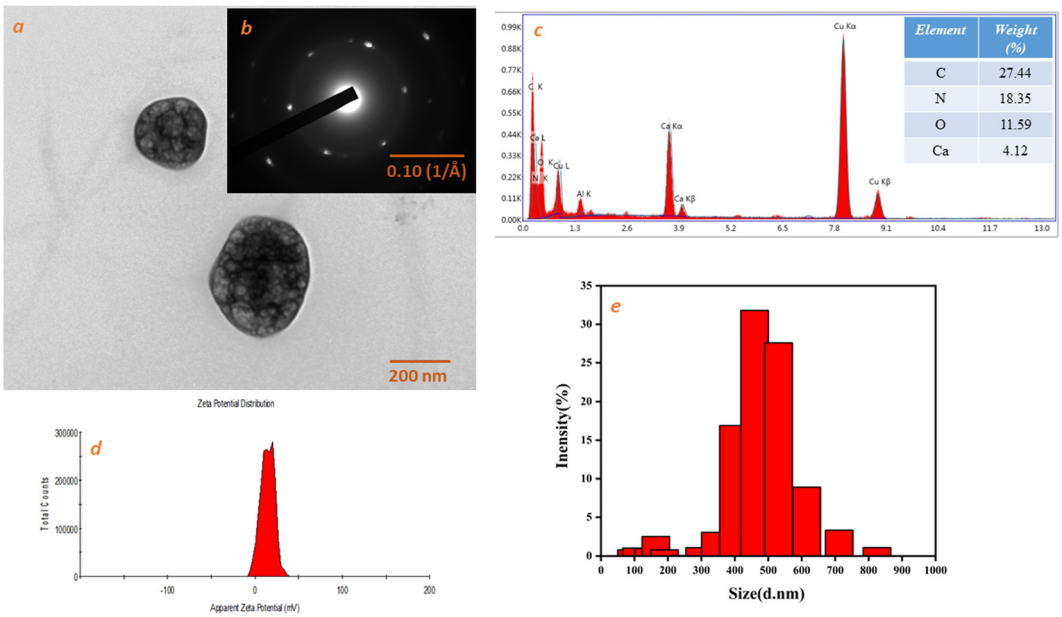

Fig. 4 (a) TEM image of Ca-MOF. (b) Diffraction pattern (inset of Fig. 4(a)). (c) EDS spectra of Ca-MOF. (d) Zeta potential of Ca-MOF. (e) Size distribution by intensity.

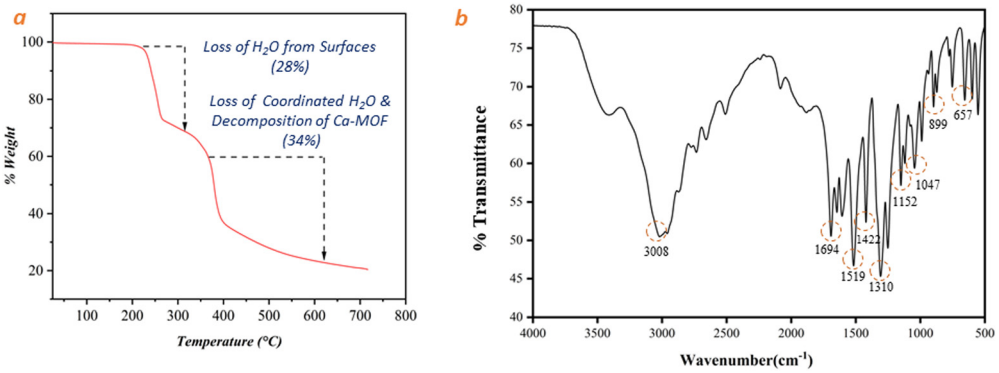

Fig. 5 (a) Thermogram (TGA) of Ca-MOF and (b) FTIR spectra of Ca-MOF.

suggest the existence of O–H stretching *via* hydrogen bonding with water and CaO, whereas the bending mode of the undissociated water molecule is detected at 1694 cm^{-1}.[27,46] The peaks at 1519 cm^{-1} correspond to asymmetric O–C–O stretch, while the peaks at 1422 cm^{-1} and 1310 cm^{-1} correspond to symmetric O–C–O stretch.[47,48] The sharp peaks depicted in Fig. 5(b) at 1694 cm^{-1} and 1422 cm^{-1} correspond to an O–C–O stretch with a bidentate bridge caused by an ionic carbonyl bond. Similarly, peaks at 657 cm^{-1} and 899 cm^{-1} imply the existence of Ca–O stretching as a component of the calcium oxo cluster[27,49]

Fig. 6 displays the nitrogen adsorption isotherm of the Ca-MOF. The adsorption and desorption curves display a typical intermediate mode between the type-III and V isotherms according to IUPAC, which indicates non-porous.[50] The textural properties of the as-synthesized MOFs are presented in Table 3. A BET surface area of 7.486 m^2 g^{-1} was observed for Ca-MOF. The pore volume and pore diameter were 0.028 cm^3 g^{-1} and 60 nm, respectively.

The average particle size and zeta potential were measured using a Zetasizer ZS 90. The size distribution by intensity and zeta potential distribution for Ca-MOF are shown in Fig. 4(e) and (d), respectively. The prepared Ca-MOF has an average particle size of 218.8 nm with a polydispersity index of 0.52. The zeta potential value of the MOF is +8.11 mV, which represents the net positive charge on the Ca-MOF.

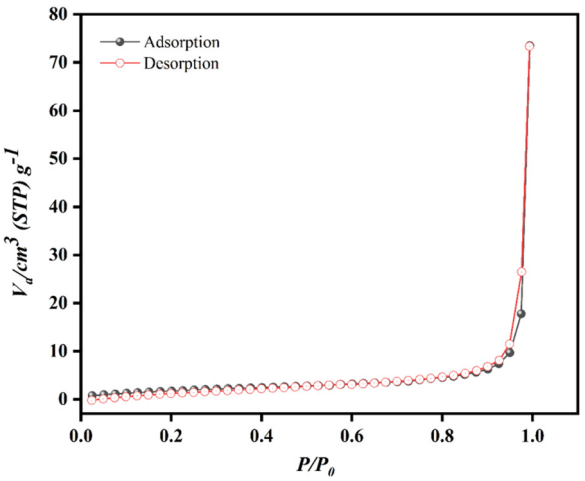

Fig. 6 Adsorption–desorption isotherm of Ca-MOF.

Table 3 Textural properties of synthesized Ca-MOF through BET analysis

MOFs	Specific surface area (SA_{BET}) (m^2 g^{-1})	Pore volume (V_{Pore}) (cm^3 g^{-1})	Average pore diameter (D_{pore}) (nm)
Ca-MOF	7.486	0.028	60

Biocompatibility studies

The possibility of damage and change in morphology (size and shape) of red blood cells in the presence of test material (Ca-MOF) was studied *via* haemolysis studies and cell integrity studies (using Giemsa staining, respectively). As shown in Fig. 7, there was no change in the shape of erythrocytes after incubation with Ca-MOF compared to the control, which was native blood, suggesting that the prepared Ca-MOF had no undesirable effect on the blood cells. The release of haemoglobin into plasma due to damage to erythrocyte membranes,[29] which is evaluated in haemolysis studies, also showed the harmless effect of the synthesised MOF.

The assay was performed according to the standard practice for assessment of haemolytic properties of materials from the American Society for Testing and Materials (ASTM F756-00, 2000); the standard classifies the materials as non-haemolytic (0–2)% of haemolysis.[29] The negative control in this study was an isotonic solution (PBS), and distilled water was taken as a positive control as osmotic stress creates ruptures of red blood cells, resulting in complete lysis. The percentage of haemolysis (Table 4) produced by Ca-MOF was observed to be around 1.55%, which is well within the acceptable limit. Overall, these observations suggest that the synthesized Ca-MOF has no undesirable effect and hence can be considered haemo-compatible.

Cell viability assay

The *in vitro* cytotoxicity of Ca-MOF was checked against fibroblast cell (L929) and human epithelial (A549) carcinoma cell lines using a well-established study, *i.e.*, MTT assay. The different concentrations of Ca-MOF in the range of 30–1000 μg ml^{-1} significantly affected the viability of normal cell lines, *i.e.*, L929 and A549 cells, as

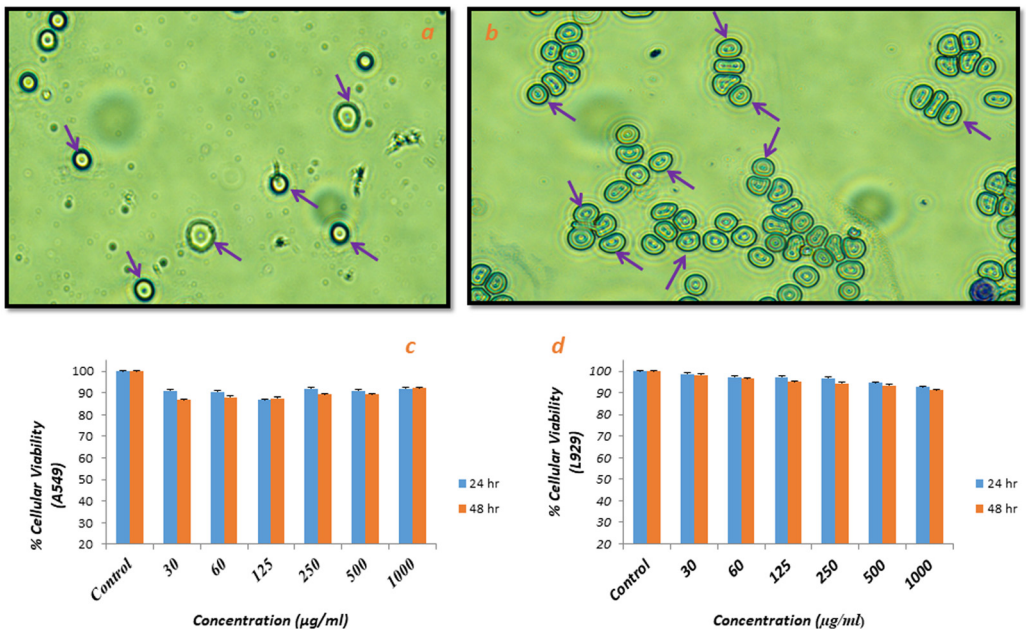

Fig. 7 Light microscopy images by Giemsa Staining Method (a) control, (b) treated with Ca-MOF (note: arrows indicate blood cell integrity), (c) cell viability assay of Ca-MOF in A549 after 24 h and 48 h and (d) cell viability assay of Ca-MOF in L929 after 24 h and 48 h.

shown in Fig. 7(c) and (d). After 24 h and 48 h of treatment, the Ca-MOF was found to be non-cytotoxic to normal cells and tumour cells at almost all concentrations. This indicates that the as-synthesized Ca-MOF did not cause significant cell death and had no cytotoxicity.

In vitro protein interaction studies

Fluorescence quenching is a technique for studying the interaction of proteins with ligands. Quenching can be either static or dynamic. Static quenching occurs when the fluorophore and the material form a nonfluorescent complex through a stable interaction. This quenching mechanism is typically associated with strong binding interactions, such as electrostatic interactions or covalent binding, between the fluorophore and the material. Dynamic quenching occurs when the fluorescence of the fluorophore is quenched through collisional encounters with the material in general. Both processes are not mutually exclusive, but the predominance is observed during the protein–ligand/material binding studies. In the Ca-MOF-protein-bioconjugate system, the intensity of the native protein originates from tryptophan, a tyrosine amino acid that is taken as an intrinsic fluorophore in the proteins, and the Ca-MOF is considered a quencher. Based on the different values obtained through measurements and calculations, it is correlated with which protein shows the highest binding with the Ca-MOF. The fluorescence emission spectra show that all the proteins show emission in the range of 320–335 nm (Fig. S1, ESI†). The maximum fluorescence intensity in all the proteins is approximately around 330 ± 5 nm, indicating that the microenvironment around tryptophan/tyrosine is changing. It is further observed that by increasing the concentration of Ca-MOF, there is a decrease in the intensity of the florescence emission peak, thereby indicating the interaction between the protein and Ca-MOF. A minor blue shift in the fluorescence intensity peak is generally observed for all the proteins, which is a reliable indicator of the protein structure function study.

Table 4 % Haemolysis studies of Ca-MOF

Samples	Absorbance at 540%	Haemolysis
Water	3.601	
PBS	0.406	
Ca-MOF	0.462	1.55

The obtained fluorescence quenching data were then used for the Stern Volmer plot. (Fig. 8). The value of the Stern–Volmer constant, K_{SV}, was determined from the slope of the Stern–Volmer plot. As can be seen from the Stern Volmer study, the K_{SV} (Stern Volmer quenching constant) value for each of the proteins, namely HSA, fibrinogen, plasminogen and gamma globulin, is given in Table 5 using eqn (2).

The trend line, as shown in the Stern–Volmer plot (Fig. 8), indicates that the Ca-MOF has a high quenching capacity. Because the K_q values are lower than 10^9 L mol^{-1} s^{-1} compared to those for static quenching, which is of the order of 10^{10} L mol^{-1} s^{-1}, as the intensity of the fluorescence peak is constantly decreasing with increasing concentrations of Ca-MOF and the Stern Volmer plots do not show a linear slope, it seems that the quenching process here is a combined static and dynamic process.

To determine the values for the binding parameters (K_a and n) for Ca-MOF and all the protein interactions, the double logarithmic equation was used (eqn (3)). The obtained fluorescence quenching data was fitted into it. The double logarithmic plot between log (F_0 − F)/F *versus* log[Q] is shown in (Fig. 9).[35] The values of K_a and n for the different proteins (Table 5) were obtained from the intercept and slope of the linear plot, respectively. As shown in Table 5, the

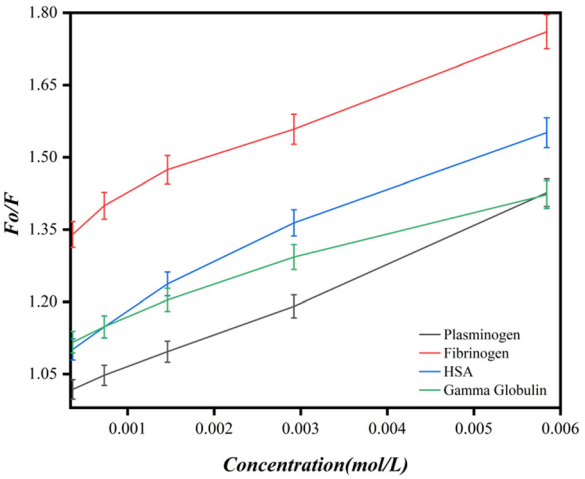

Fig. 8 The Stern–Volmer plot of different proteins with an increasing concentration of Ca-MOF.

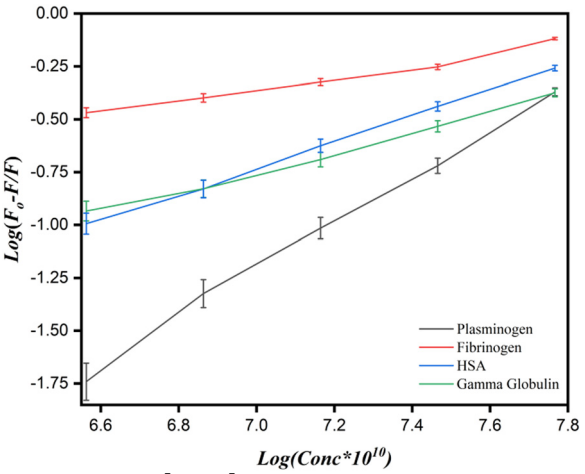

Fig. 9 The plot of $\log\left[\frac{F_0 - F}{F}\right]$ *vs.* log [MOFs] for proteins conjugate with Ca-MOF.

association constant is highest for the plasminogen with the highest number of binding sites ($8.0 \pm 0.1 \times 10^5$ L mol^{-1} and 1.1116 ± 0.05, respectively). Although we can say that there is interaction of the Ca-MOF with all the other proteins, the most prominent interaction is with Plasminogen.

Ex vivo studies

Haemostatic performance of Ca-MOF. To understand the effect on hemostasis, the clotting time of Ca-MOF was measured, as depicted in Fig. 10. The observed clotting time of 5 s for Ca-MOF was significantly lower compared to clotting time in the control, *i.e.*, 240 s, (Fig. 10(a)), indicating the role of Ca-MOF in the process. After clot formation, it was observed that the Ca-MOF appeared to be aggregated with a much larger dimension of 2 μm, which could be due to swelling and platelet aggregation. As shown in Fig. 10(b), some platelets seem to adhere to the surface of Ca-MOF. Additionally, the plasma recalcification time (PRT) test was performed by taking the synthesized Ca-MOF with platelet poor plasma (PPP) to evaluate the material effect on the intrinsic coagulation factors. It is well known that the longer the PRT, the better the anticoagulant property. As compared to the major influence observed on the clotting time, the reduction in the PRT was much less owing to Ca-MOF (approx. 90% of control values, $p < 0.01$) as shown in Fig. 11(a). These results were supported by examining the SEM micrographs of platelet adhesion to Ca-MOF (Fig. 11(b)). The platelets were observed to assume a polygonal morphology on the MOF surfaces compared to the normal discoid shape, indicating their spreading on the matrix and leading to the activation of platelet plug formation.

To evaluate the effect of Ca-MOF on clotting, a TEG analysis was performed. The clotting ability of the test sample, *i.e.* Ca-MOF at various concentrations, was measured in whole blood. The *R* and *K* values due to Ca-MOF were lower than those of whole blood, as illustrated in Table 6, whereas α and MA were significantly higher. The synthesised Ca-MOF was found to considerably shorten the time between the start of coagulation and the synthesis of fibrinogen with improved polymerization, clot stability, and overall clot strength. The blood spiked with Ca-MOF solutions in a tris buffer (pH 7.4) at final concentrations ranging from 250 to 1000 μg ml^{-1} revealed shorter *R* and *K*. (Fig. 12). The concentration of 500 μg ml^{-1} of the Ca-MOF showed the most pronounced changes in all the parameters (namely, *R*, *K*, α, MA, and *G*) compared to the control (native citrated blood). At higher concentrations of Ca-MOF, the *R* and *K* values, which are expected to be lower, increased and the MA value, which was expected to be higher, decreased.

This might indicate the reverse behaviour of the Ca-MOF setting in. This is possible as it is known that when there is an excess of calcium ions in the blood, the ions can bind to and inactivate the clotting proteins, thus preventing the formation of blood clots. Therefore, increasing the concentration of calcium ions in the blood can have an anticoagulant effect by interfering with the normal clotting process. This might make the material useful for a different set of medical conditions, which involve preventing blood clots in patients at high risk of thromboembolism.

Table 5 Binding characteristics of Ca-MOF: protein interaction, as studied in PBS, with pH 74

Temp. (K)	Name of protein	$K_{sv} \times 10^5$ (L mol^{-1})	$K_q \times 10^9$ (L mol^{-1} s^{-1})	$K_a \times 10^5$ (L mol^{-1})	*n*
298	HSA	80.0 ± 0.1	8.08 ± 0.1	5.0 ± 0.05	0.61861 ± 0.1
	Fibrinogen	73.0 ± 0.05	7.31 ± 0.05	2.0 ± 0.1	0.28053 ± 0.1
	Plasminogen	73.0 ± 0.05	7.4± 0.05	8.0 ± 0.1	1.1116 ± 0.05
	Gamma globulin	55.0 ± 0.1	5.51 ± 0.05	4.0 ± 0.05	0.47047 ± 0.05

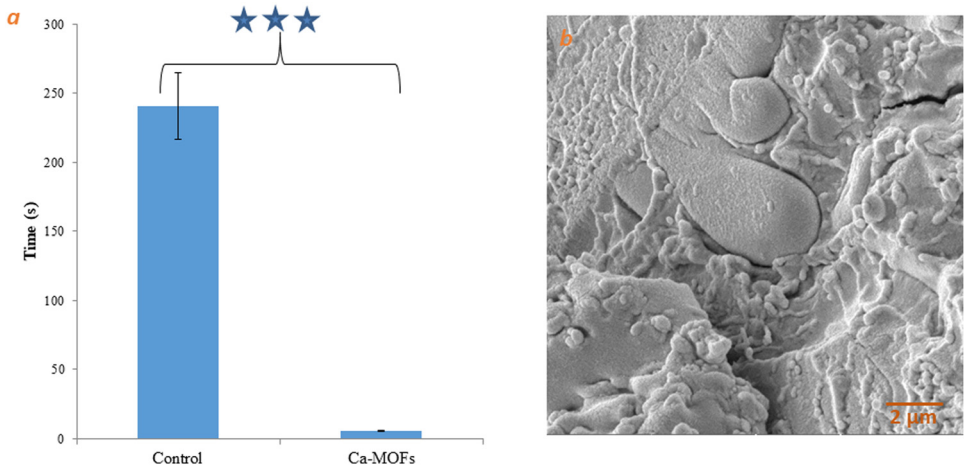

Fig. 10 (a) Whole blood clotting time of Ca-MOF. (b) SEM image of Ca-MOF in contact with human whole blood. Note: *** indicates significance.

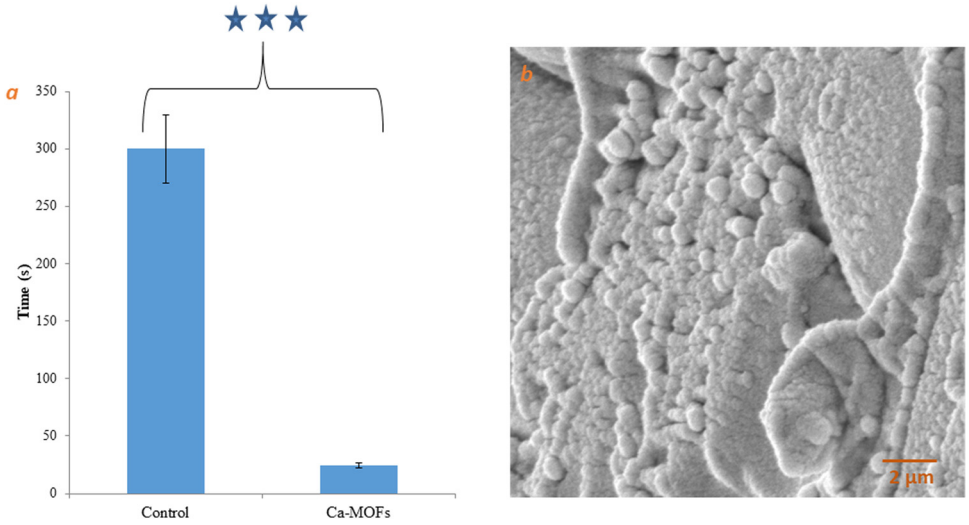

Fig. 11 (a) Plasma recalcification time of Ca-MOF. (b) Plasma adhesion on the surface of Ca-MOF. Note: *** indicates significance.

Table 6 The coagulation performance of Ca-MOF by thromboelastography

Sample	Concn (μg ml^{-1})	*R* (Minute)	*K* (Minute)	α (Degree)	MA (mm)	*G* (kd sc^{-1})
Ca-MOF	Control	8.3 ± 0.05	6.9 ± 0.05	30.3 ± 0.1	35.4 ± 0.05	2.7 ± 0.1
	1000	6.3 ± 0.1	5.2 ± 0.05	38.0 ± 0.1	36.9 ± 0.1	2.9 ± 0.05
	500	***5.2 ± 0.05***	***3.5 ± 0.1***	***47.8 ± 0.1***	***43.3 ± 0.1***	***3.8 ± 0.05***
	250	5.8 ± 0.1	4.2 ± 0.05	43.4 ± 0.2	39.6 ± 0.05	3.3 ± 0.1

Note: all the values presented in this table are in the form of mean ± SD.

In vivo studies

A well-established rat-tail amputation model was used to evaluate the *in vivo* hemostatic effect of Ca-MOF. The comparison of the properties was done with the clinically used hemostatic drug, tranexamic acid.[51] The shortest clotting time was achieved by Ca-MOF, *i.e.* (39 ± SD s), followed by tranexamic acid (89 ± SD s) compared to (300 ± SD s) s for the control (Fig. 13(a) and (b)). The weights of blood loss found due to Ca-MOF, tranexamic acid and control were (0.14 ± SD g), (0.38 ± SD g) and (1.06 ± SD g), respectively. This *in vivo* study proved that Ca-MOF has a better ability to bring about rapid hemostasis.

Co-relative analysis

The aim of this study was to prepare a bio-MOF where the individual components, *i.e.*, the metal and the linker, are biocompatible, and to investigate the effect they may have on

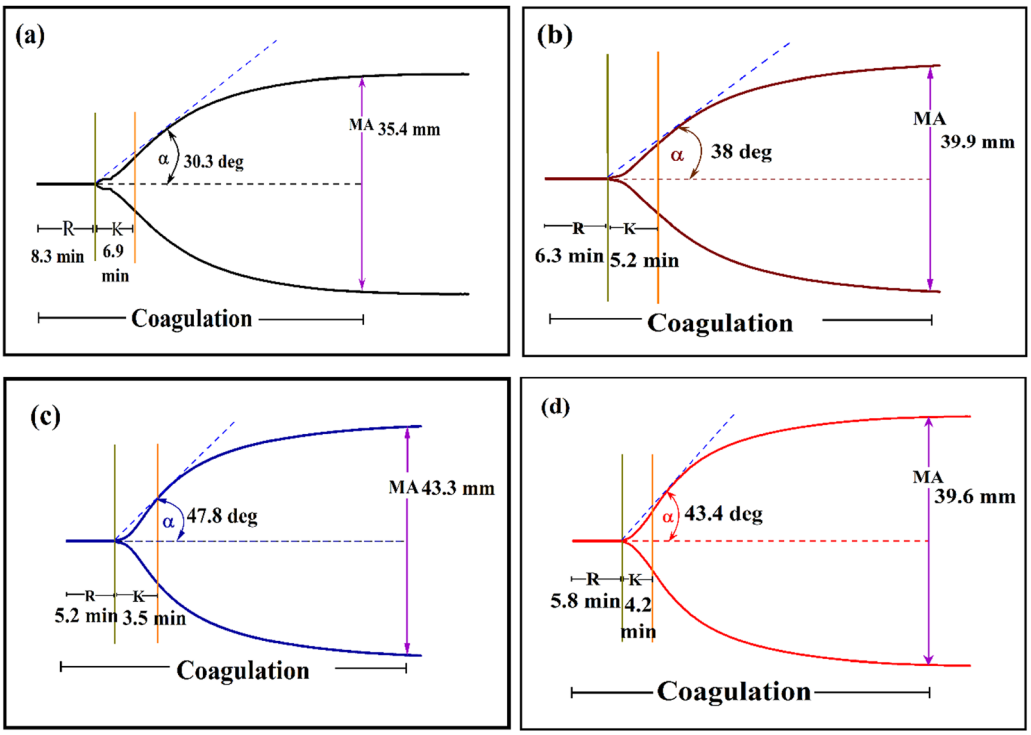

Fig. 12 Thermboelastogram of (a) control (native blood), (b) 1000 μg ml^{-1} of Ca-MOF, (c) 500 μg ml^{-1} of Ca-MOF and (d) 250 μg ml^{-1} of Ca-MOF.

the hemostatic property. Thus, calcium and aspartic acid were taken both of which have their known individual roles in the biological system.[44] Calcium is also well known for its role in the coagulation system, but very few MOFs of calcium have been explored for this application owing to their difficult synthesis and lower yields. Using the box Behnken method, we zeroed down on the conditions that could give the highest yield. However, under these conditions, porosity, and surface area are not high. The Ca-MOF forms plate-like structures that have a 3D morphology and influence the hemostatic property.

A correlative analysis of the interaction of Ca-MOF with the blood is presented here using the TEG study, which provides very useful information about global hemostasis, from the beginning of coagulation through clot formation to the ending with fibrinolysis. The effect seems concentration dependent as the best results are observed at a concentration of 500 μg ml^{-1}. The initial results show that the clotting time of the control is 240 s while that of the Ca-MOF is 5 s. This was a highly significant difference that we wanted to check before reporting. As we evaluated the coagulation cascade (Fig. 14), we started plotting the parameters across the intrinsic and extrinsic pathways involved in interacting with Ca-MOF. The effect starts with the reaction time [*R*], which is reduced by approximately 37%, from 8.3 in the control to 5.2 when treated with Ca-MOF, thereby implying the interaction with coagulation factors VII and VIIa. The coagulation time [*K*] rate of clot strengthening, which is associated with the activity of the intrinsic clotting factors, fibrinogen and platelets, decreases compared to the control. However, the maximum amplitude [MA], which indicates the maximum strength of the clot, increases by 18%, which is a

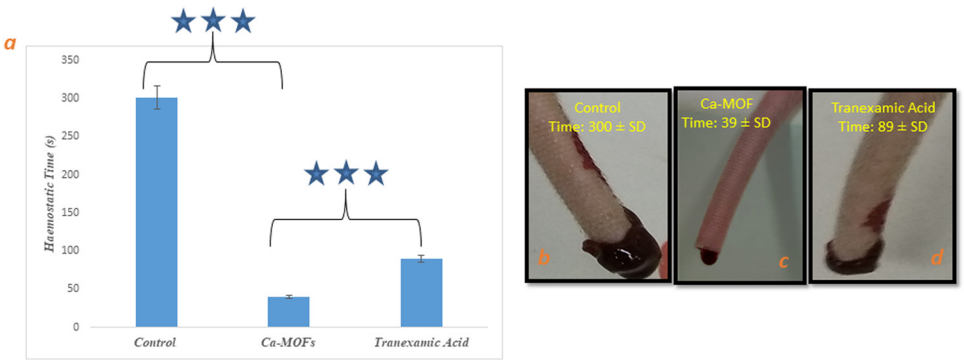

Fig. 13 (a) Haemostatic time of Ca-MOF, (b) tail bleeding image of control, (c) tail bleeding image of Ca-MOF, (d) tail bleeding image of standard (tranexamic acid). Note: *** indicates significance.

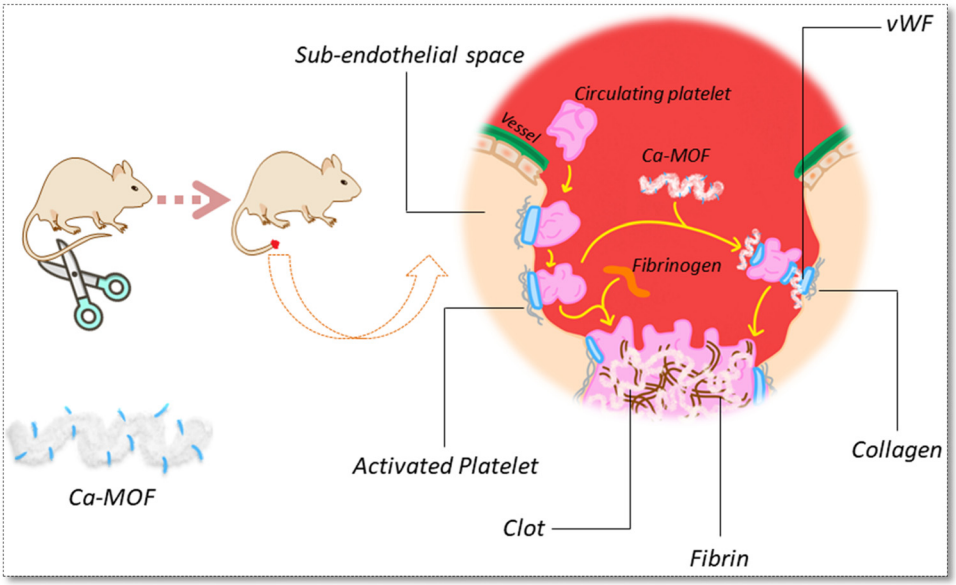

Fig. 14 Proposed interaction of the Ca-MOF within the coagulation cascade.

direct function of the maximum dynamic properties of fibrin and platelet number and functions. The rate of clot polymerization, *i.e.* α angle, which is a main function of platelets, fibrinogen, and plasma components residing on the platelet surface, increases by 36% compared to the control. The *G* value may also identify the relative contributions of clotting factors, such as fibrinogen and platelets, to the overall coagulation process, which also increases Ca-MOF. It is also seen in protein binding studies that the interaction of the Ca-MOF is more with plasminogen. Simultaneously, this could possibly be the reason for the Ca-MOF showing anticoagulant behaviour at higher (1000 μg ml^{-1}) concentrations. When an injury occurs and blood clotting is initiated, plasminogen is activated to plasmin, which is an enzyme responsible for fibrinolysis, and the breakdown of blood clots. It can bind to fibrin and prevent excessive clotting by inhibiting the formation of additional clots. This makes the material very novel because it seems to have both a coagulating capacity at a lower concentration and anticoagulant property at a higher concentration. However, further extensive studies on these aspects will be required to confirm the same. The evaluated Ca-MOF showed the shortest clotting time (39 ± 02 s) and lowest blood loss (0.14 ± 0.2 g) in the rat-tail amputation model compared to the control and commercially available haemostatic drug tranexamic acid. Thus, we can see that the best results for this MOF are obtained at a concentration of 500 μg ml^{-1} at which it acts as a potential bio-MOF-based haemostat.

Conclusion

In this study, Ca-MOF was designed for the management of severe bleeding during military and civilian trauma. The as-synthesized Ca-MOF under optimized conditions effectively absorbs fluid and activates the adsorption and aggregation of red blood cells, as observed in the SEM image. In addition, the calcium core of the Ca-MOF activated the intrinsic pathway of the coagulation cascade, which leads to promoting blood clotting and achieving haemorrhage control *in vitro* and *in vivo*. More importantly, Ca-MOF showed superior biocompatibility as observed during the haemolysis and cell integrity studies. We believe that this finding showcases the haemostatic potential of Ca-MOF for the first time and provides an alternative treatment option for haemorrhage control using this bio-MOF.

Disclosures

Human subjects

Consent was obtained by all participants in this study. Institutional Ethics Committee at Institute of Nuclear Medicines & Allied Sciences, New Delhi issued approval (ECR/824/Inst/DL/2016/RR-19).

Animal studies

All animal experiments were performed as per protocol approved by the institutional ethical committee (INM/IAEC/19/01/Ext.1 dated 02-09-21).

Author contributions

C. B. J.: synthesis and writing original draft. C. S.: software design studies, R. V.: methodology S. S.: data curation, K. M.: dupervision and resources, R. M.: conceptualised and planned all the experiments, and supervised the entire project.

Conflicts of interest

The authors declare that they have no known conflict of interest of any kind.

Acknowledgements

The authors show gratitude for the constant support of Director INMAS during this work. We also acknowledge the help taken from the central instrumentation facility at IIT, Delhi, to carry out some of the characterisation studies. The first author is thankful to DRDO for the financial support extended as SRF.

References

1 M. X. Wu and Y. W. Yang, *Adv. Mater.*, 2017, **29**, 1–20.
2 A. C. McKinlay, R. E. Morris, P. Horcajada, G. Férey, R. Gref, P. Couvreur and C. Serre, *Angew. Chem., Int. Ed.*, 2010, **49**, 6260–6266.
3 M. Yu, D. You, J. Zhuang, S. Lin, L. Dong, S. Weng, B. Zhang, K. Cheng, W. Weng and H. Wang, *ACS Appl. Mater. Interfaces*, 2017, **9**, 19698–19705.
4 D. Chen, D. Yang, C. A. Dougherty, W. Lu, H. Wu, X. He, T. Cai, M. E. Van Dort, B. D. Ross and H. Hong, *ACS Nano*, 2017, **11**, 4315–4327.
5 H. Furukawa, N. Ko, Y. B. Go, N. Aratani, S. B. Choi, E. Choi, A. Ö. Yazaydin, R. Q. Snurr, M. O'Keeffe, J. Kim and O. M. Yaghi, *Science*, 2010, **329**, 424–428.
6 R. J. Drout, L. Robison and O. K. Farha, *Coord. Chem. Rev.*, 2019, **381**, 151–160.
7 M. Giménez-Marqués, T. Hidalgo, C. Serre and P. Horcajada, *Coord. Chem. Rev.*, 2016, **307**, 342–360.
8 P. Horcajada, R. Gref, T. Baati, P. K. Allan, G. Maurin and P. Couvreur, *Chem. Rev.*, 2012, 1232–1268.
9 C. Tamames-Tabar, A. García-Márquez, M. J. Blanco-Prieto, C. Serre and P. Horcajada, *MOFs in Pharmaceutical Technology*, 2014, vol. 9783527335.
10 M. Mon, J. Ferrando-Soria, T. Grancha, F. R. Fortea-Pérez, J. Gascon, A. Leyva-Pérez, D. Armentano and E. Pardo, *J. Am. Chem. Soc.*, 2016, **138**, 7864–7867.
11 D. Banerjee, H. Wang, B. J. Deibert and J. Li, *Chem. Met. Fram. Synth. Charact. Appl.*, 2016, 73–103.
12 W. E. Rauser, *Cell Biochem. Biophys.*, 1999, **31**, 19–48.
13 S. D. Bennett, B. A. Core, M. P. Blake, S. J. A. Pope, P. Mountford and B. D. Ward, *Dalton Trans.*, 2014, **43**, 5871–5885.
14 D. S. Auld, *Biometals*, 2001, **14**, 271–313.
15 S. L. Anderson and K. C. Stylianou, *Coord. Chem. Rev.*, 2017, **349**, 102–128.
16 R. Vaidhyanathan, D. Bradshaw, J. N. Rebilly, J. P. Barrio, J. A. Gould, N. G. Berry and M. J. Rosseinsky, *Angew. Chem., Int. Ed.*, 2006, **45**, 6495–6499.
17 E. V. Anokhina, Y. B. Go, Y. Lee, T. Vogt and A. J. Jacobson, *J. Am. Chem. Soc.*, 2006, **128**, 9957–9962.
18 J. P. Barrio, J. N. Rebilly, B. Carter, D. Bradshaw, J. Bacsa, A. Y. Ganin, H. Park, A. Trewin, R. Vaidhyanathan, A. I. Cooper, J. E. Warren and M. J. Rosseinsky, *Chem. – Eur. J.*, 2008, **14**, 4521–4532.
19 J. A. Gould, J. Bacsa, H. Park, J. B. Claridge, A. M. Fogg, V. Ramanathan, J. E. Warren and M. J. Rosseinsky, *Cryst. Growth Des.*, 2010, **10**, 2977–2982.
20 J. A. Gould, J. T. A. Jones, J. Bacsa, Y. Z. Khimyak and M. J. Rosseinsky, *Chem. Commun.*, 2010, **46**, 2793–2795.
21 L. Antolini, G. Marcotrigiano, L. Menabue, G. C. Pellacani and M. Saladini, *Inorg. Chem.*, 1982, **21**(6), 2263–2267.
22 P. Kulkarni and D. Rawtani, *J. Pharm. Sci.*, 2019, **108**, 2643–2653.
23 M. Can, S. Demirci, A. K. Sunol and N. Sahiner, *Microporous Mesoporous Mater.*, 2020, **309**, 110533.
24 S. Wang, M. Wahiduzzaman, J. Marrot, C. Martineau-corcos, S. Devautour-vinot, C. Serre, L. Davis, A. Tissot, W. Shepard, D. Hamdane and G. Maurin, *Nat. Commun.*, 2018, 1–8.
25 B. Ruozi, D. Belletti, M. A. Vandelli, F. Pederzol, P. Veratti, F. Forni, G. Tosi, M. Tonelli and M. Zapparoli, *J. Phys. Chem. Biophys.*, 2014, **4**(4), DOI: **10.4172/2161-0398.1000150**.
26 G. Gizer, M. Sahiner, Y. Yildirim, S. Demirci, M. Can and N. Sahiner, *Curr. Res. Green Sustainable Chem.*, 2021, **4**, 100110.
27 P. George, R. K. Das and P. Chowdhury, *Microporous Mesoporous Mater.*, 2019, **281**, 161–171.
28 A. K. Bajpai, R. Bhatt and R. Katare, *Micron*, 2016, **90**, 12–17.
29 Z. Mirzakhanian, K. Faghihi, A. Barati and H. R. Momeni, *J. Biomater. Sci., Polym. Ed.*, 2015, **26**, 1439–1451.
30 R. Luna-Vázquez-gómez, M. E. Arellano-García, J. C. García-Ramos, P. Radilla-Chávez, D. S. Salas-Vargas, F. Casillas-Figueroa, B. Ruiz-Ruiz, N. Bogdanchikova and A. Pestryakov, *Materials*, 2021, **14**(11), 2792.
31 S. I. Kaba and E. M. Egorova, *Nanotechnol. Sci. Appl.*, 2015, **8**, 19–29.
32 K. Satyavani, S. Gurudeeban, T. Ramanathan and T. Balasubramanian, *Avicenna J. Med. Biotechnol.*, 2012, **4**, 35–39.
33 N. Gligorijević, M. Radomirović, A. Rajković, O. Nedić and T. Ć. Veličković, *Foods*, 2020, **9**(6), 780.
34 X. J. Shi, D. Li, J. Xie, S. Wang, Z. Q. Wu and H. Chen, *Chin. Sci. Bull.*, 2012, **57**, 1109–1115.
35 A. A. Roian and S. Tayyab, *Biochem. Mol. Biol. Educ.*, 2019, **47**, 156–160.
36 P. Sasmal and P. Datta, *J. Drug Delivery Sci. Technol.*, 2019, **52**, 559–567.
37 W. Janvikul, P. Uppanan, B. Thavornyutikarn, J. Krewraing and R. Prateepasen, *J. Appl. Polym. Sci.*, 2006, **102**, 445–451.
38 W. Everett, D. J. Scurr, A. Rammou, A. Darbyshire, G. Hamilton and A. De Mel, *Sci. Rep.*, 2016, **6**, 1–12.
39 J. Vincent Edwards, E. Graves, N. Prevost, B. Condon, D. Yager, J. Dacorta and A. Bopp, *Pharmaceutics*, 2020, **12**, 1–19.
40 H. T. Peng, *Mater. Sci. Eng. Adv. Res.*, 2016, **1**, 1–7.
41 M. Liu, J. Yang, J. Guan, S. Huang, Z. Li and M. Jing, *Ad. Eng. Res.*, 2018, **146**, 229–234.
42 H. T. Peng, M. D. Blostein and P. N. Shek, *Clin. Appl. Thromb./Hemostasis*, 2012, **18**, 27–34.
43 C. Lv, L. Li, Z. Jiao, H. Yan, Z. Wang, Z. Wu, M. Guo, Y. Wang and P. Zhang, *Bioact. Mater.*, 2021, **6**, 2346–2359.
44 F. Chen, X. Cao, X. Chen, J. Wei and C. Liu, *J. Mater. Chem. B*, 2015, **3**, 4017–4026.
45 A. K. Gaharwar, R. K. Avery, A. Assmann, A. Paul, G. H. Mckinley, A. Khademhosseini and B. D. Olsen, *ACS Nano*, 2014, **8**, 9833–9842.

46 M. Signoretto, V. Nichele, E. Ghedini, F. Pinna and G. Cerrato, *One-step synthesis of silica gel used in the controlled release of drug*, Elsevier B.V., 2008, vol. 174.
47 L. Q. Wei, J. Y. Lu, Q. Q. Li, Y. Zhou, L. Le Tang and F. Y. Li, *Inorg. Chem. Commun.*, 2017, **78**, 43–47.
48 M. Nara, H. Morii and M. Tanokura, *Biochim. Biophys. Acta, Biomembr.*, 2013, **1828**, 2319–2327.
49 C. J. Lee, C. S. Nah, C. S. Teng, W. W. Jun and M. Saravanan, *Chem. Pap.*, 2015, **69**, 1325–1330.
50 M. Thommes, K. Kaneko, A. V. Neimark, J. P. Olivier, F. Rodriguez-Reinoso, J. Rouquerol and K. S. W. Sing, *Pure Appl. Chem.*, 2015, **87**, 1051–1069.
51 Y. Gao, A. Sarode, N. Kokoroskos, A. Ukidve, Z. Zhao, S. Guo, R. Flaumenhaft, A. Sen Gupta, N. Saillant and S. Mitragotri, *Sci. Adv.*, 2020, **6**, 1–13.